

The Python Sky Model: software for simulating the Galactic microwave sky

B. Thorne¹, J. Dunkley¹, D. Alonso¹, S. Næss¹

¹*Department of Physics, University of Oxford, Keble Road, Oxford OX1 3RH*

10 August 2016

ABSTRACT

We present a numerical code to simulate maps of Galactic emission in intensity and polarization at microwave frequencies, aiding in the design of Cosmic Microwave Background experiments. This Python code builds on existing efforts to simulate the sky by providing an easy-to-use interface and is based on publicly available data from the *WMAP* and *Planck* satellite missions. We simulate synchrotron, thermal dust, free-free, and anomalous microwave emission over the whole sky, in addition to the Cosmic Microwave Background, and include a set of alternative prescriptions for the frequency dependence of each component that are consistent with current data. We also present a prescription for adding small-scale realizations of these components at resolutions greater than current all-sky measurements. The code is available at https://github.com/bthorne93/PySM_public.

Key words: cosmology: cosmic background radiation – cosmology: observations

1 INTRODUCTION

In recent years the temperature and polarization anisotropies of the Cosmic Microwave Background (CMB) have been measured with increasing precision by the *WMAP* and *Planck* satellites (Hinshaw et al. 2013; Planck Collaboration et al. 2015a), coupled with ground and balloon-based observations. The constraints these observations place on the parameters that describe the cosmology of the Universe have been tight enough to usher in the era of ‘precision cosmology’.

Further progress will be made by measuring the polarization anisotropies of the CMB to greater precision. It is in the power spectrum of these anisotropies that the signature of primordial gravitational waves may be found, which would provide strong evidence in support of the scenario that the Universe went through an early period of inflation (e.g., Baumann et al. 2009). Current polarization data are starting to provide the strongest constraints on primordial gravitational waves (BICEP2/Keck and Planck Collaborations et al. 2015).

The CMB temperature anisotropy dominates over foreground emission from the Galaxy in a broad range of frequencies. In contrast, the polarized CMB signal is weaker than the strongly polarized Galactic thermal dust and synchrotron radiation. In particular, the divergence-free B -mode polarization signal sourced by primordial gravitational waves at recombination is predicted to be at least several orders of magnitude weaker than the polarized foregrounds,

averaged over the sky, and is a subdominant signal even in the cleanest sky regions (Planck Collaboration et al. 2015c).

To optimize our ability to extract the CMB polarization signal from upcoming and future experiments we rely on realistic models of the Galactic emission to simulate observations of these components at a range of frequencies. Several sky simulation tools are already publically available, including the Planck Sky Model (Delabrouille et al. 2013) and the Global Sky Model (de Oliveira-Costa et al. 2008; Zheng et al. 2016). While our work was in preparation a similar modeling and software effort was presented in Hervías-Caimapo et al. (2016) for polarized Galactic emission.

With the new code presented here we build on existing efforts, providing a flexible and easily used tool for simulating Galactic emission that includes recent public data from the *Planck* satellite. We do not attempt to physically model the emission in three dimensions, via for example, integrating a dust or electron density over a Galactic magnetic field (e.g. Waelkens et al. 2009; Fauvet et al. 2011, 2012; Jansson & Farrar 2012; Orlando & Strong 2013; Beck et al. 2014). Instead we adopt empirical models that describe the frequency scaling of each component with simple forms consistent with current data, using high signal-to-noise maps of each component as templates at frequencies far from the foreground minimum. These simulations are therefore limited in scope and will not capture the complexity present in the true emission.

The structure of this paper is as follows: in §2 we describe the structure of the code together with the models and alternatives used for each component. In §3 we describe

a procedure to add small-scale anisotropy to the simulated maps; and in §4 we summarize the usefulness and limitations of these simulations.

2 LARGE-SCALE SIMULATIONS

We simulate Galactic diffuse emission in intensity and polarization from four Galactic components: thermal dust, synchrotron, free-free, and anomalous microwave emission (AME). We also include a gravitationally lensed CMB realization and white instrument noise. Maps can be integrated over a top-hat bandpass describing the response of each experimental channel, and smoothed with a Gaussian beam.

The user specifies a set of observation frequencies, beam widths, bandpass widths, noise and chosen output components and units. The code simulates each component at each frequency using a phenomenological model. One or more emission template maps are defined at pivot frequencies, and then the extrapolation in frequency is performed using scaling laws and maps of spectral parameters. A lensed CMB realization can be included by calling the `Taylens` software (Naess & Louis 2013) directly, or using a pre-calculated realization. The software is designed to be easily extendable to alternative models or scalings. The intensity and polarized emission as a function of frequency for the models we consider is summarized in Figure 1, together with the template maps in Figure 2.

2.1 Synchrotron

Synchrotron radiation is the dominant radiation mechanism in polarization at frequencies $\lesssim 50$ GHz (e.g., Kogut et al. 2007). It is produced by cosmic rays spiralling around Galactic magnetic fields and radiating. The power and spectral energy distribution depends on both the strength of the local magnetic field, and the energy distribution of the injected cosmic rays. The polarization of the radiation depends on the orientation of the intervening magnetic field. The predicted dependence of the spectrum on the magnetic field for a population of cosmic rays with energy distribution $N(E) \propto E^{-p}$ is, in antenna temperature units:

$$I_\nu \propto B^{\frac{p+1}{2}} \nu^\beta, \quad (1)$$

where $\beta = -\frac{(p+3)}{2}$ (B. Rybicki & P. Lightman 1979). The spectral index, β , is expected to have some spatial variability and to vary with frequency. As synchrotron sources age their spectral energy distribution (SED) steepens, since high frequency radiation corresponds to higher energy particles which radiate energy away most rapidly. Along a line of sight there will likely also be multiple synchrotron components, and the stacking of their spectra can lead to flattening of the SED. The spectrum can also be flattened through effects of synchrotron self-absorption, which tends to be more significant towards the Galactic center.

2.1.1 Model 1: Nominal index

The nominal PySM model assumes that the synchrotron intensity is a scaling of the degree-scale-smoothed 408 MHz

Haslam map (Haslam et al. 1981; Haslam et al. 1982), reprocessed by Remazeilles et al. (2014). It models the polarization as a scaling of the WMAP 9-year 23 GHz Q and U maps (Bennett et al. 2013), smoothed to three degrees. Both of these maps have small scales added using the prescription described in §3.

In the nominal model we simulate the spectral index as being a power-law in every direction, such that

$$I_\nu^{\text{Synch}}(\hat{\mathbf{n}}) = A_{\nu_0}(\hat{\mathbf{n}}) \left(\frac{\nu}{\nu_0} \right)^{\beta_s(\hat{\mathbf{n}})}. \quad (2)$$

As in the nominal Planck Sky Model v1.7.8 simulations, we use the spectral index map from ‘Model 4’ of Miville-Deschenes et al. (2008), calculated from a combination of Haslam and WMAP 23 GHz polarization data using a model of the Galactic magnetic field. We assume that the index is the same in temperature and polarization, although the true sky will most likely be more complicated than this. The template maps and index map are shown in Fig 2.

2.1.2 Model 2: Spatially steepening index

The cosmic rays responsible for synchrotron radiation are thought to be energized by processes such as supernovae, which are more common in the Galactic plane. Synchrotron emission observed at higher latitudes will therefore likely be produced by older cosmic rays which have diffused out of the Galactic plane, and therefore lost more energy. This is expected to result in the steepening of the synchrotron spectral index away from the plane (Kogut 2012; Ichiki 2014). Evidence for steepening in the polarization emission has been seen in Kogut et al. (2007); Fuskeland et al. (2014); Ruud et al. (2015) using WMAP and QUIET data.

We parameterize the steepening with a smoothly varying index described by a gradient δ_β that scales with Galactic latitude, b , such that $\beta_s = \beta_{s,b=0} + \delta_\beta \sin|b|$. In Model 2 we use $\delta_\beta = -0.3$, consistent with WMAP polarization data Kogut et al. (2007). The simulated index varies from $\beta_s = -3.0$ at the equator to $\beta_s = -3.3$ at the poles in both intensity and polarization, as shown in Figure 2.

2.1.3 Model 3: Curvature of index

The synchrotron emission may be better modelled by a curved spectrum that either flattens or steepens with frequency. Model 3 simulates the steepening or flattening of the spectral index above a frequency, ν_c as:

$$I_\nu^{\text{Synch}}(\hat{\mathbf{n}}) = A_{\nu_0}(\hat{\mathbf{n}}) \left(\frac{\nu}{\nu_0} \right)^{\beta_s(\hat{\mathbf{n}}) + C \ln(\frac{\nu}{\nu_c})}, \quad (3)$$

where positive C corresponds to flattening and negative C to steepening.

Kogut (2012) fits this model to a small patch of sky with ten overlapping radio frequency sky surveys and WMAP 23 GHz data, finding best-fit values of $\beta = -2.64 \pm 0.03$, $C = -0.052 \pm 0.005$ at 0.31 GHz. This corresponds to a steepening of about 0.57 between 408 MHz and 94 GHz. Evaluating the spectral index at 23 GHz Kogut (2012) finds $\beta_{23} = -3.09 \pm 0.05$. This is consistent with the index map in model 1 which has a mean and standard deviation of

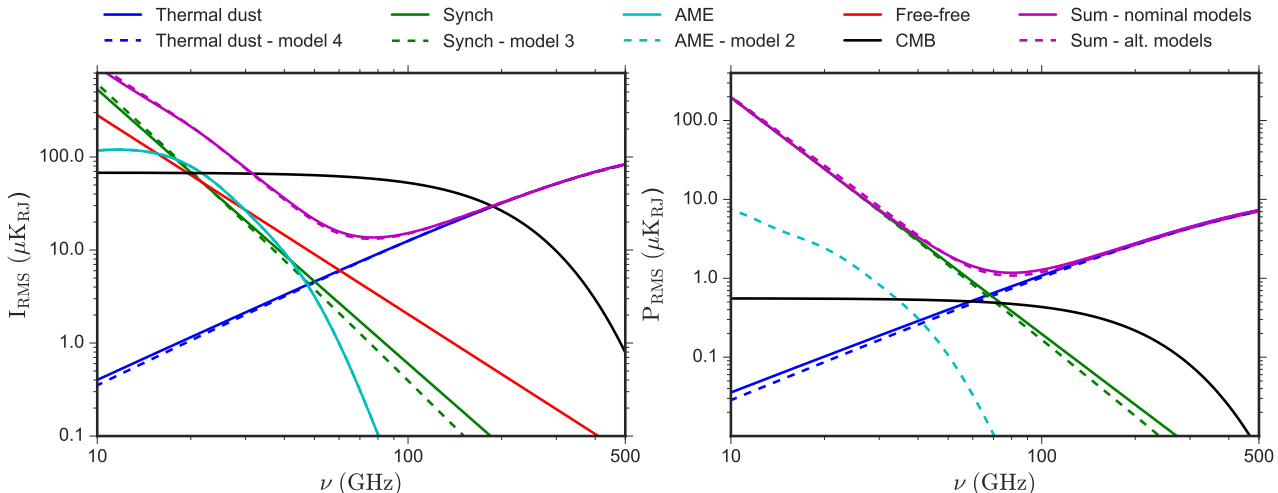


Figure 1. The frequency scaling laws for the individual components of PySM; we show the nominal and alternative models as solid and dashed lines respectively. We show only the alternative models which have a significant impact on the shape of the spectrum. These spectra are calculated by producing masked maps of each component at each frequency, smoothing to FWHM 1° in intensity and $40'$ in polarization, and then computing the RMS. The mask used in intensity is the WMAP 9 year KQ85 mask, and the polarization mask is the *Planck* polarization confidence mask CPM83.

-3.00 ± 0.06 . Therefore, for simplicity we use the same map as model 1 from Miville-Deschenes et al. (2008) for $\beta(\hat{\mathbf{n}})$, and a baseline curvature value of $C = -0.052$ at $\nu_c = 23$ GHz.

2.2 Thermal dust emission

At frequencies greater than ≈ 70 GHz the polarized foreground spectrum is dominated by thermal dust emission. The dust grains are thought to be a combination of carbonaceous and silicate grains, and polycyclic aromatic hydrocarbons (PAHs). The total emission results from the interaction of these species with the interstellar radiation field: the grains are heated by absorption in the optical and cool by emitting in the far infrared (e.g., Draine 2011). The thermal dust is polarized since aspherical dust grains preferentially emit along their longest axis, which tend to align perpendicular to magnetic fields.

In the frequency range of interest for CMB experiments, the spectrum is well approximated by a modified blackbody with a power-law emissivity, such that

$$I = A\nu^{\beta_d} B_\nu(T_d), \quad (4)$$

for spectral index β_d and temperature T_d , where B_ν is the Planck function. A single component at $T = 15.9$ K fits the *Planck* data well (Planck Collaboration et al. 2015b), with different indices preferred by the intensity ($\beta = 1.51 \pm 0.01$) and polarization (1.59 ± 0.02) data. This difference indicates the presence of multiple components with different polarization properties.

In intensity the two component model of Finkbeiner et al. (1999), with a hot and cold component at 9.4 K and 16 K, is marginally preferred (Meisner & Finkbeiner 2014). They use this model to extrapolate 100 μm emission and 100/240 μm flux ratio maps to microwave frequencies. The exact physical model is not well constrained by current observations, including the number of components, spatial

variability of spectral index, and spatial variation of the dust temperature.

2.2.1 Model 1: Nominal index

Our nominal model uses template maps at 545 GHz in intensity and 353 GHz in polarization. We use the templates estimated from the *Planck* data using the ‘Commander’ code (Planck Collaboration et al. 2015b). In polarization these maps closely match the 353 GHz *Planck* data which is dominated by thermal dust. We use the N_{side} 2048 dust intensity map degraded to N_{side} 512, and the polarization product smoothed to two degrees FWHM in polarization with small scale variations added by the procedure described in section §3.

In the nominal simulations, we model the frequency scaling as a single component, using the best-fit emissivity estimated by the Commander fit. The emission model is given by

$$\begin{aligned} I_\nu^d(\hat{\mathbf{n}}) &= A_{I,\nu_I}(\hat{\mathbf{n}})(\nu/\nu_I)^{\beta_d(\hat{\mathbf{n}})} B_\nu(T_d(\hat{\mathbf{n}})) \\ \{Q_\nu^d(\hat{\mathbf{n}}), U_\nu^d(\hat{\mathbf{n}})\} &= \{A_{Q,\nu_P}(\hat{\mathbf{n}}), A_{U,\nu_P}(\hat{\mathbf{n}})\} \times \\ &\quad (\nu/\nu_P)^{\beta_d(\hat{\mathbf{n}})} B_\nu(T_d(\hat{\mathbf{n}})) \end{aligned} \quad (5)$$

Here $\nu_I = 545$ GHz and $\nu_P = 353$ GHz. We assume that the intensity and polarization share the same index, as was assumed in the Commander fitting process. Both β_d and T_d vary spatially; the maps are shown in Fig 2.

This model will not capture all the of the physical complexity as it is likely that silicate and carbonaceous grains have distinct emissivities. They also likely have different degrees of polarization, since the efficiency of the grain alignment varies with the size and shape of grain. This would result in the polarization fraction in dust being a function of frequency, with some evidence for this shown in Planck Collaboration et al. (2015c).

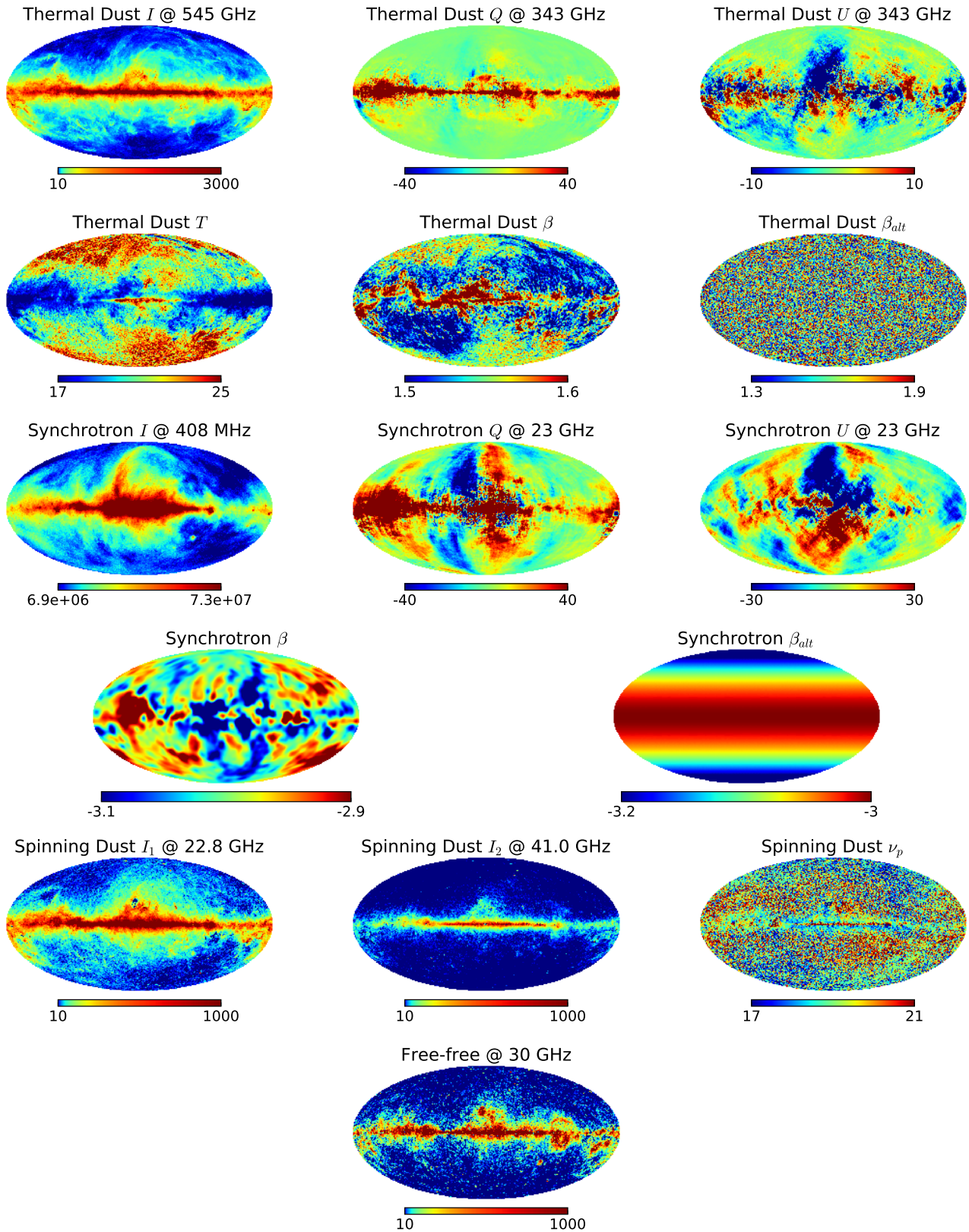


Figure 2. Template maps used in the PySM models. All emission templates are in units of μK_{RJ} and all dust temperature templates are in K. Intensity templates are plotted on a log scale, and the polarization templates on a linear scale.

Model	Mean	Std. Dev.
Nominal	1.53	0.22
$\sigma(\beta) = 0.2$	1.58	0.24
$\sigma(\beta) = 0.3$	1.58	0.23
Uniform	1.58	0.23

Table 1. Statistics of dust polarization index calculated from different simulations of dust polarization at 217 GHz and 353 GHz containing instrumental noise compatible with the corresponding *Planck* channels.

2.2.2 Models 2 and 3: Spatially variable index

The dust index is expected to vary spatially, in particular in polarization, but current data cannot strongly constrain this possible variation. We perform a test to assess how well a varying index can be detected by the *Planck* data given the current noise levels.

We simulate a spectral index map with degree-scale variation drawn from a Gaussian of mean 1.59 and dispersion σ . We then simulate polarized dust emission in Stokes Q and U at 217 and 353 GHz at $N_{\text{side}} = 128$ for σ in the range 0.05 to 0.7. We produce noise maps at 217 GHz and 353 GHz using the *Planck* half-mission full-sky maps at 217 and 353 GHz. We first degrade these to $N_{\text{side}} 128$ and then at each frequency take the difference of the two half-mission maps and divide by a factor of 2. Finally we smooth each noise map with a Gaussian kernel of one degree FWHM. We then estimate the index from these maps in circles of radius ten degrees centred on Healpix $N_{\text{side}} = 8$ pixels, using

$$\beta_d(\hat{\mathbf{n}}) = \frac{\ln\left(\frac{[Q,U]_1(\hat{\mathbf{n}}) B(\nu_2, T(\hat{\mathbf{n}}))}{[Q,U]_2(\hat{\mathbf{n}}) B(\nu_1, T(\hat{\mathbf{n}}))}\right)}{\ln\left(\frac{\nu_2}{\nu_1}\right)} + 2. \quad (6)$$

This follows a similar method used in the comparable *Planck* analysis in [Planck Collaboration et al. \(2015c\)](#), except we do not use the 143 GHz channel and do not add CMB and synchrotron, nor fit for them. We use a similar region as the *Planck* analysis, shown in Fig 4. The dispersion of the indices for a uniform input index of 1.59, and for an input index map with degree-scale variation of standard deviation of 0.2 is shown in Figure 3, and can be compared to Figure 9 in [Planck Collaboration et al. \(2015c\)](#). The statistics of the recovered index distributions for these two models, the nominal model, and a model with a larger standard deviation of 0.3, are shown in Table 1.

The distributions for β_d are similar since the data are noise-dominated. The dispersion due to noise is ~ 0.22 compared to the value of 0.17 found in [Planck Collaboration et al. \(2015c\)](#), and the value of 0.22 found in a comparable calculation by [Poh & Dodelson \(2016\)](#). This indicates that models of the dust spectral index with significant spatial variation on degree scales are still consistent with the data. Furthermore, a recent analysis of decorrelation of the *Planck* half-mission and detector set maps found an intrinsic variation of 0.07 in the dust index ([Planck Collaboration et al. 2016](#)). Models 2 and 3 therefore modify the nominal dust model with a different spectral index map. The spectral index of model 2 (3) is a Gaussian random field with mean of 1.59 and $\sigma = 0.2(0.3)$ varying on degree scales for both intensity and polarization.

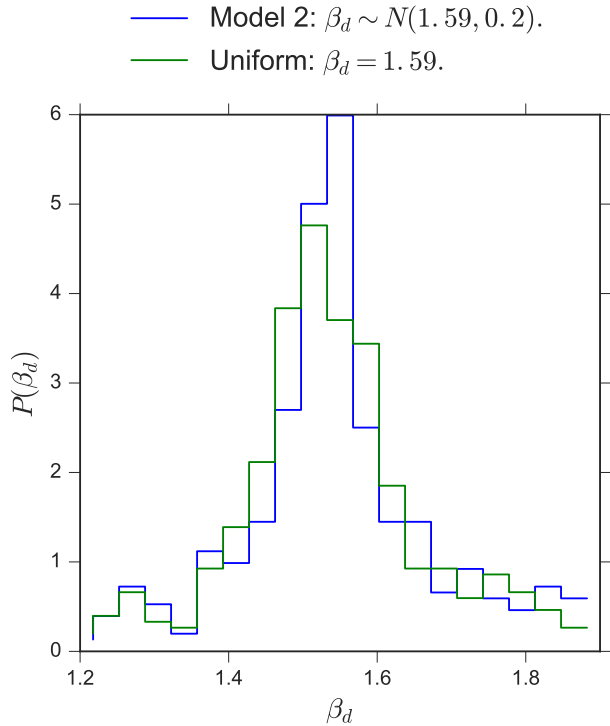


Figure 3. Normalized histograms of the dust spectral index, β_d , calculated for noisy simulations of different PySM models with varying intrinsic index dispersion. We see that the resulting dispersions are very similar, indicating noise-dominated data.

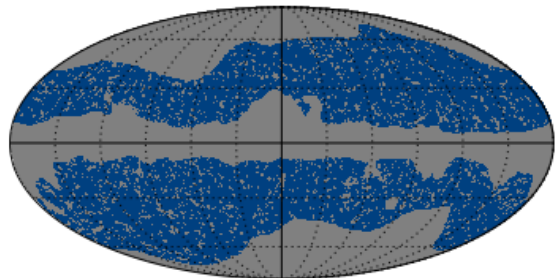


Figure 4. Mask used in calculation of β_d in section 2.2.2. This mask is an approximation to the one used in the *Planck* analysis (figure 1 of [Planck Collaboration et al. \(2015c\)](#)).

2.2.3 Model 4: Two dust temperatures

One can also consider a number N_d of dust components with their own temperatures and spectral indices:

$$I(\hat{\mathbf{n}}, \nu) = \sum_{a=1}^{N_d} I_a(\hat{\mathbf{n}}) \left(\frac{\nu}{\nu_*}\right)^{\beta_a} \frac{B_\nu(T_a(\hat{\mathbf{n}}))}{B_{\nu_*}(T_a(\hat{\mathbf{n}}))}, \quad (7)$$

and similarly for polarization. For our fourth dust model we use $N_d = 2$, using the best-fit model templates estimated by [Meisner & Finkbeiner \(2014\)](#) from the *Planck* data, using the model from [Finkbeiner et al. \(1999\)](#).

The model as proposed in these references can be writ-

ten as

$$I(\hat{\mathbf{n}}, \nu) = I_{\nu_0}(\hat{\mathbf{n}}) \frac{\sum_{a=1}^2 f_a q_a \left(\frac{\nu}{\nu_0}\right)^{\beta_a} B_\nu(T_a(\hat{\mathbf{n}}))}{\sum_{b=1}^2 f_b q_b B_{\nu_0}(T_b(\hat{\mathbf{n}}))}, \quad (8)$$

where I_{ν_0} is the intensity template at 100 μm ($\nu_0 = 3000$ GHz), β_k are constant spectral indices, T_k are spatially varying dust temperatures, q_k is the IR/optical ratio for each species, f_k is the fraction of power absorbed from the interstellar radiation field and emitted in the FIR by each component, and we have omitted the color correction factors. In order to adapt this to the model in Eq. 7 we generate the separate amplitude templates $I_a(\hat{\mathbf{n}})$, at $\nu_* = 545$ GHz in terms of I_{ν_0} and $T_k(\hat{\mathbf{n}})$ as

$$I_a(\hat{\mathbf{n}}) = I_{\nu_0}(\hat{\mathbf{n}}) \frac{\left(\frac{\nu_*}{\nu_0}\right)^{\beta_a} f_a q_a B_{\nu_*}(T_a(\hat{\mathbf{n}}))}{\sum_{b=1}^2 f_b q_b B_{\nu_0}(T_b(\hat{\mathbf{n}}))}. \quad (9)$$

In polarization, we construct the polarization simulations using the polarization angles and fractional polarization from the 353 GHz template maps in Model 1, such that

$$\begin{aligned} Q(\nu, \hat{\mathbf{n}}) &= f_d(\hat{\mathbf{n}}) I(\nu, \hat{\mathbf{n}}) \cos(2\gamma(\hat{\mathbf{n}})) \\ U(\nu, \hat{\mathbf{n}}) &= f_d(\hat{\mathbf{n}}) I(\nu, \hat{\mathbf{n}}) \sin(2\gamma(\hat{\mathbf{n}})). \end{aligned} \quad (10)$$

where $f_d = \sqrt{Q^2 + U^2}/I$ at 353 GHz in Model 1.

2.3 Anomalous microwave emission

Anomalous microwave emission refers to emission with a spectral distribution not well approximated by known foreground models. It has been detected in compact objects, and in the diffuse sky, with early measurements by [de Oliveira-Costa et al. \(1997\)](#); [Leitch et al. \(1997\)](#). It is spatially correlated with dust, and primarily important in the 20 - 40 GHz range, with variable peak frequency ([Stevenson 2014](#)).

A likely model for the emission is rapidly spinning dust grains. [Draine & Lazarian \(1998\)](#) explain the emission by a population of grains of size $< 3 \times 10^{-7}$ cm, with modest electric dipole moments. A candidate for these grains is polycyclic aromatic hydrocarbons (PAHs) that are detected in vibrational emission in the range 3 – 12 μm . The theoretical SED for such spinning PAH grains have been successfully fit to AME observations ([Hoang et al. 2011](#)), but recent analysis of the *Planck* data has cast some doubt on their nature ([Hensley et al. 2015](#)). A second candidate for AME is magnetic dipole radiation due to thermal fluctuations of magnetization in small silicate dust grains ([Draine & Lazarian 1999](#)).

2.3.1 Model 1: Nominal unpolarized AME

We model the AME using the *Planck* templates derived from the *Commander* parametric fit to the *Planck* data ([Planck Collaboration et al. 2015b](#)), using the *Commander* model:

$$\begin{aligned} I_\nu^{\text{AME}}(\hat{\mathbf{n}}) &= A_{\nu_{0,1}}(\hat{\mathbf{n}}) \epsilon(\nu, \nu_{0,1}, \nu_{p,1}(\hat{\mathbf{n}}), \nu_{p0}) \\ &+ A_{\nu_{0,2}}(\hat{\mathbf{n}}) \epsilon(\nu, \nu_{0,2}, \nu_{p,2}, \nu_{p0}). \end{aligned} \quad (11)$$

Here the first component has a spatially varying emissivity, and the second component a spatially constant emissivity. Both these emissivity functions are calculated using

SpDust2 ([Ali-Haimoud et al. 2009](#); [Silsbee et al. 2011](#)), evaluated for a cold neutral medium and shifted in $\log(\nu) - \log(I)$ space. The two template maps are shown in Figure 2. This nominal AME model is unpolarized.

2.3.2 Model 2: Polarized AME

AME is not thought to be strongly polarized, and the polarization fraction has been constrained to be below 1 - 3% in the range 23 - 41 GHz by observations of the Perseus molecular complex using *WMAP* 7-year data ([Dickinson et al. 2011](#)). More recent observations of AME emission from the molecular complex W43 by the QUIJOTE experiment have placed a 0.39% upper limit on its polarization fraction, which falls to 0.22% when combined with *WMAP* data ([G enova-Santos et al. 2016](#)). [Remazeilles et al. \(2016\)](#) found that neglecting a 1% level of polarized AME can bias the derived value of the tensor-to-scalar ratio by non-negligible amounts for satellite missions.

To construct a template we use the dust polarization angles, γ_d , calculated from the *Planck Commander* 2015 thermal dust Q and U maps at 353 GHz. The AME polarization is then

$$Q_a = f_a I_\nu \cos(2\gamma_{353}), \quad U_a = f_a I_\nu \sin(2\gamma_{353}). \quad (12)$$

In this model we assign a global polarization fraction of 2%; the fraction can also be easily changed by varying the f_a parameter.

2.4 Free-free

Free-free emission is caused by electrons scattering off ions in the interstellar medium ([B. Rybicki & P. Lightman 1979](#)). The frequency scaling is well approximated by a function of the electron temperature and emission measure ([Draine 2011](#)). This is very close to a power law of -2.14 at frequencies greater than 1 GHz, and flattens abruptly at lower frequencies ([Planck Collaboration et al. 2015b](#)).

Free-free has been measured in *WMAP* and *Planck* intensity data, and it should be unpolarized since the scattering is independent of direction. However, there are small effects at the edges of dense ionized clouds due to the non-zero quadrupole moment in the electron temperature, which can cause up to 10% polarization (e.g., [Fraisse et al. 2009](#)). The net polarization over the sky is estimated to be below 1% ([Macellari et al. 2011](#)).

The *PySM* nominal model for free-free emission assumes it is unpolarized, and uses the degree-scale smoothed emission measure and effective electron temperature *Commander* templates ([Planck Collaboration et al. 2015b](#)). We apply the analytic law presented in [Draine \(2011\)](#) to produce an intensity map at 30 GHz, which we then scale with a spatially constant power law index. We choose this index to be -2.14 consistent with *WMAP* and *Planck* measurements for electrons at ~ 8000 K ([Bennett et al. 2013](#); [Planck Collaboration et al. 2015b](#)). This gives

$$I_\nu^{\text{ff}}(\hat{\mathbf{n}}) = A_{\nu_0}^{\text{ff}}(\hat{\mathbf{n}}) \left(\frac{\nu}{\nu_0}\right)^{-2.14}. \quad (13)$$

Different behaviour will be expected below ~ 0.01 GHz,

where the `Commander` model flattens (Planck Collaboration et al. 2015b).

2.5 CMB

We use the `Taylens` code (Næss & Louis 2013) in `PySM` to generate a lensed CMB realization. The input to `Taylens` is a set of C_l 's ($C_{TT}, C_{EE}, C_{BB}, C_{TE}, C_{\phi\phi}, C_{T\phi}, C_{E\phi}$) which have been calculated using the `CAMB` numerical code (Lewis et al. 2000). The nominal model uses Λ CDM cosmological parameters that best fit the *Planck* 2015 data. We incorporate the functions of `Taylens` into the `PySM` code for portability, so some functionality is removed¹. We scale the CMB emission between frequencies using the blackbody function.

The user can opt to either run `Taylens` during the simulation, or use a pre-computed temperature and polarization map supplied with the code or generated by the user. If using `Taylens`, the CMB map can also be artificially delensed, with the expected lensing signal suppressed by a chosen factor.

2.6 Instrument

We describe the instrument response with a simple top-hat bandpass, Gaussian white noise, and Gaussian beam profile. The user specifies a central frequency, ν , and a width per band, $\Delta\nu$. The output signal is calculated using

$$I_{\nu, \Delta\nu}(\hat{\mathbf{n}}) = \int_{\nu - \frac{\Delta\nu}{2}}^{\nu + \frac{\Delta\nu}{2}} \frac{I_{\nu'}(\hat{\mathbf{n}})}{\Delta\nu} d\nu'. \quad (14)$$

The white noise level is set per band for both intensity and polarization. The beam is characterized by a FWHM per channel. This instrument model will not capture realistic noise realizations or realistic bandpasses; the code is designed to be easily modifiable to incorporate such features.

3 SMALL-SCALE SIMULATIONS

Ground-based CMB experiments often observe only small patches of sky, and current data limit how well we can predict the small-scale behaviour of the foregrounds in high latitude regions at the $\ell \sim 100$ scales of interest. Here we describe our method for simulating sky maps at a higher resolution than the available data. Our approach is to extrapolate the angular power spectrum of the available data to smaller scales, drawing a Gaussian realization from this spectrum. Other similar methods have been implemented in Miville-Deschenes et al. (2008); Delabrouille et al. (2013); Remazeilles et al. (2014); Hervías-Caimapo et al. (2016).

We simulate intensity and polarization maps using $M = M_0 + M_{\text{ss}}$ where M_0 is the original smoothed data and M_{ss} is our small-scale simulation. We implement different methods in polarization and intensity for generating M_{ss} . Although the real sky will be non-Gaussian, we limit these small-scale simulations to Gaussian or lognormal realizations.

3.1 Polarization

The *WMAP* and *Planck* polarization templates used in `PySM` are all noise dominated at degree scales at high Galactic latitudes. To add power to the Q and U maps at small-scales we determine the multipole, ℓ_* , to which the original template is limited in resolution, smooth the maps to this scale, and add a realization of a model power law spectrum to the smoothed templates. We compute angular power spectra on masked skies using the `PolSpice` code² (Chon et al. 2004).

The scale ℓ_* varies spatially, but here we adopt a single global ℓ_* , which we determine by computing the polarization power spectra in a region centered on RA, DEC = [0, -55], chosen as the location of the BICEP2/Keck patch. We choose a square region of side 40 degrees for synchrotron, and 30 degrees for dust, with a larger region for synchrotron as the maps are noisier. We fit the spectra with a signal-plus-noise model,

$$\frac{\ell(\ell+1)}{2\pi} C_\ell^{\text{BB}} = A\ell^\gamma + N \frac{\ell(\ell+1)}{2\pi}, \quad (15)$$

approximating the uncertainties on the spectrum as due only to cosmic variance. We fit for three free parameters A , γ and N , and estimate ℓ_* as the scale at which this model is minimal in BB or EE . The masked synchrotron and dust EE and BB spectra are shown in Figures 5 and 6. We find $\ell_*^{\text{synch}} = 36$ and $\ell_*^{\text{dust}} = 69$.

We generate the large-scale templates M_0 by smoothing the original maps with a Gaussian kernel of FWHM $\theta_{\text{fwhm}} = 180/\ell_*$ deg. We then construct M_{ss} by assuming that the small-scales follow a power law behaviour with $\frac{\ell(\ell+1)}{2\pi} C_\ell^{\text{XX}} = A^{\text{XX}} \ell^{\gamma^{\text{XX}}}$. We find A^{XX} and γ^{XX} by fitting this model to the EE and BB spectra calculated on the original template with a Galactic mask. We use the *WMAP* polarization analysis mask for synchrotron (Gold et al. 2011), and the 80% mask provided in the second *Planck* data, which we refer to here as Gal80. We find $\gamma^{\text{synch,EE}} = -0.66$, $\gamma^{\text{synch,BB}} = -0.62$, $\gamma^{\text{dust,EE}} = -0.31$, $\gamma^{\text{dust,BB}} = -0.15$.

We multiply these power law spectra by the window function $1 - W_\ell(\ell_*)$, where $W_\ell = \exp(-\sigma^2(\ell_*)\ell^2)$ with $\sigma = \theta_{\text{fwhm}}/\sqrt{8 \ln(2)}$, such that it be added to the large-scale map that has been smoothed by the window function W_ℓ . We then draw a pair of Q and U Gaussian random fields, δ_G , from this spectrum using the `HEALPix`³ routine `synfast`.

We expect the true small-scale power to be modulated by the large-scale power, so we multiply the Gaussian random field by a spatially varying normalization such that

$$M_{\text{SS}} = N(\hat{\mathbf{n}})\delta_G(\hat{\mathbf{n}}). \quad (16)$$

We choose $N(\hat{\mathbf{n}})$ by dividing the sky into `Healpix` $N_{\text{side}} = 2$ pixels and computing the angular power spectrum in each patch, $C_\ell(\hat{\mathbf{n}})$, and smoothing this map with FWHM 10° to avoid sharp pixel boundaries. We define

$$N(\hat{\mathbf{n}}) = \sqrt{\frac{C_{\ell_*}(\hat{\mathbf{n}})}{A\ell_*^\gamma}} \quad (17)$$

² The `PolSpice` code is available at <http://www2.iap.fr/users/hivon/software/PolSpice/>

³ The `HEALPix` code is available at <http://healpix.sourceforge.net>

¹ The original code is available at <https://github.com/amaurea/taylens>

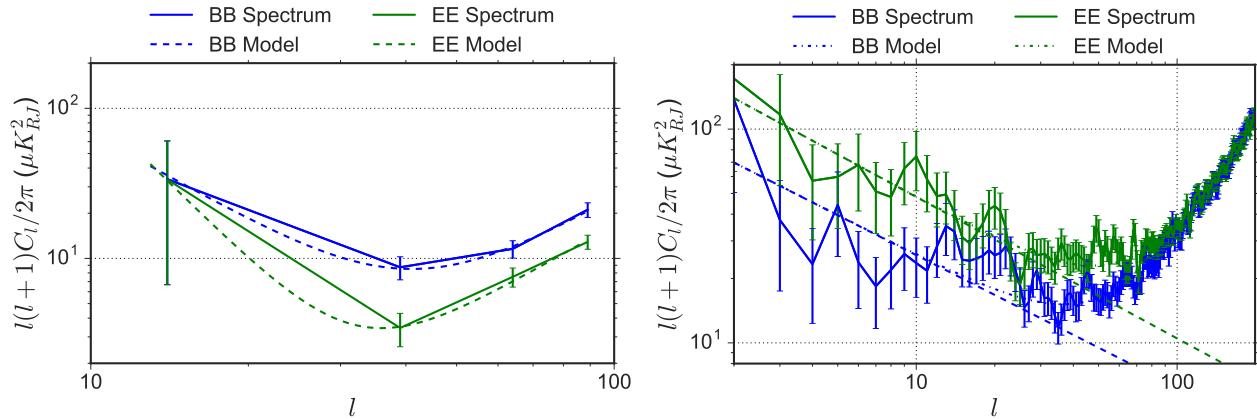


Figure 5. *Left:* synchrotron polarization spectra in a square region centered on RA, DEC = [0, -55] of size 1600 deg². The errors shown are cosmic variance only. The best-fit power-law signal plus noise model from Eqn. 15 is shown. The BB model minimum is used to estimate the scale l_* to smooth the maps. *Right:* synchrotron polarization spectra computed with the WMAP polarization analysis mask, and best-fit model. The dashed lines are the extrapolated power laws used in the small-scale simulation.

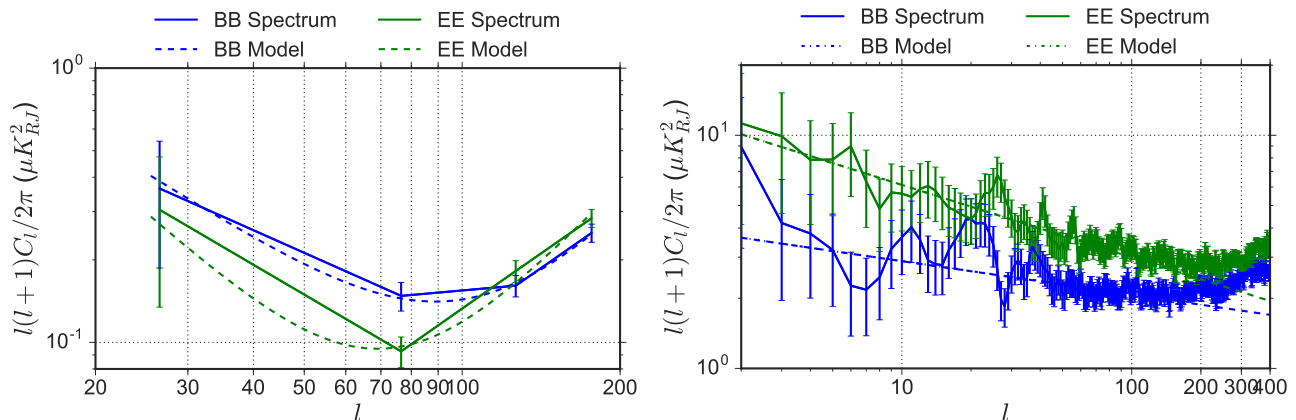


Figure 6. *Left:* dust polarization spectra as in Figure 5, but for a smaller patch of 800 square degrees. *Right:* dust polarization spectra as in Figure 5, but using the *Planck* Gal 80 Galactic plane mask.

so that the small-scale realization is normalized by the large-scale power in each patch. The $N(\hat{\mathbf{n}})$ for the dust Q template is shown in Figure 9.

A patch of the resulting Q map for dust is shown in Figure 10, illustrating the large-scale and additional small scale components. We also show the power spectra of the maps in Figures 7 and 8, both for the masked all-sky maps and the smaller regions centered at [0,-55]. In both regions the power law behaviour is continuous at $\ell = \ell_*$.

We note that a limitation of this method is that it does not capture spatial variations in the modulation of the small-scale signal on scales smaller than $N_{\text{side}}/2$ pixels, so the normalization will not be accurate in these small regions.

3.2 Intensity: Synchrotron

We use a similar procedure for simulating the intensity at small-scales, but we use a lognormal rather than Gaussian distribution because it guarantees that the final map will be positive. It is also possible to generate a lognormal distribution from a Gaussian random field, and maintain the shape of the Gaussian field's angular power spectrum to a

good approximation. In these simulations we do not impose a correlation between the intensity and polarization at small scales.

For synchrotron, the Haslam template is provided at 57 arcminute resolution, which defines M_0 . As for the polarization we fit a power law to the signal, finding $\gamma = -0.55$. We draw a Gaussian realization δ_G with variance σ_G^2 , but here we generate M_{ss} using a lognormal distribution with

$$M_{\text{ss}} = M_0^{\min} [\exp(R(\hat{\mathbf{n}})\delta_G(\hat{\mathbf{n}}) - \sigma_G^2/2) - 1]. \quad (18)$$

Here $R(\hat{\mathbf{n}})$ normalizes the small scales. Instead of using the local power spectrum, we normalize the small-scale intensity map by the large-scale intensity smoothed to 4° and raised to a power

$$R(\hat{\mathbf{n}}) = \left[\frac{M_0(\hat{\mathbf{n}})}{\langle M_0 \rangle} \right]^\alpha.$$

We find the best-fit $\alpha = 0.6$ that results in a total power spectrum of $\ell(\ell+1)C_\ell \propto \ell^\gamma$, fit in the multipole range $200 < \ell < 1000$. An example of the synchrotron maps are shown in Figure 11.

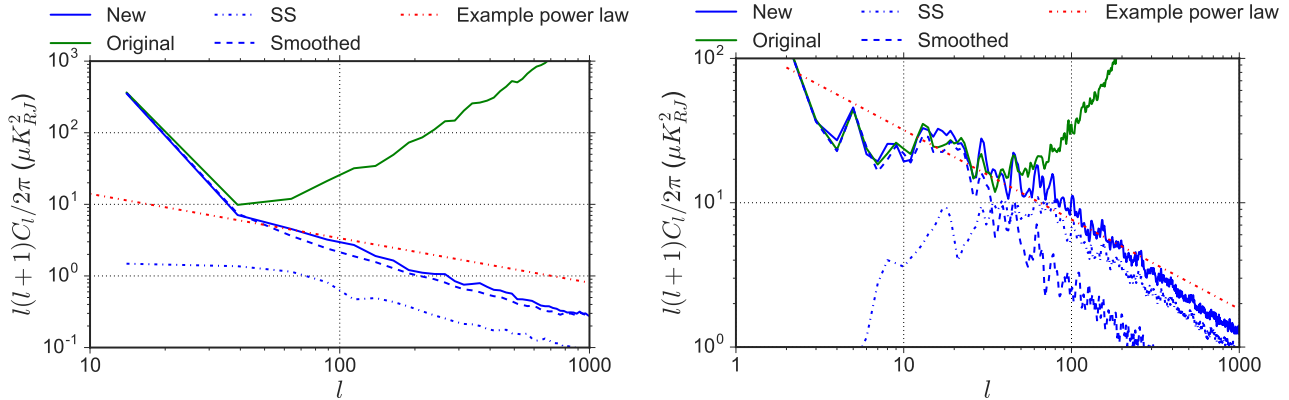


Figure 7. *Left:* synchrotron BB spectra using the 1600 square degree region centered on RA, DEC = [0, -55]. We show the original template, the smoothed template, the small scale realization, and the final map with small scales added. The dashed red line shows the shape of the power law of the small scale realization to guide the eye. *Right:* synchrotron BB spectra over 75% of the sky using the WMAP polarization analysis mask.

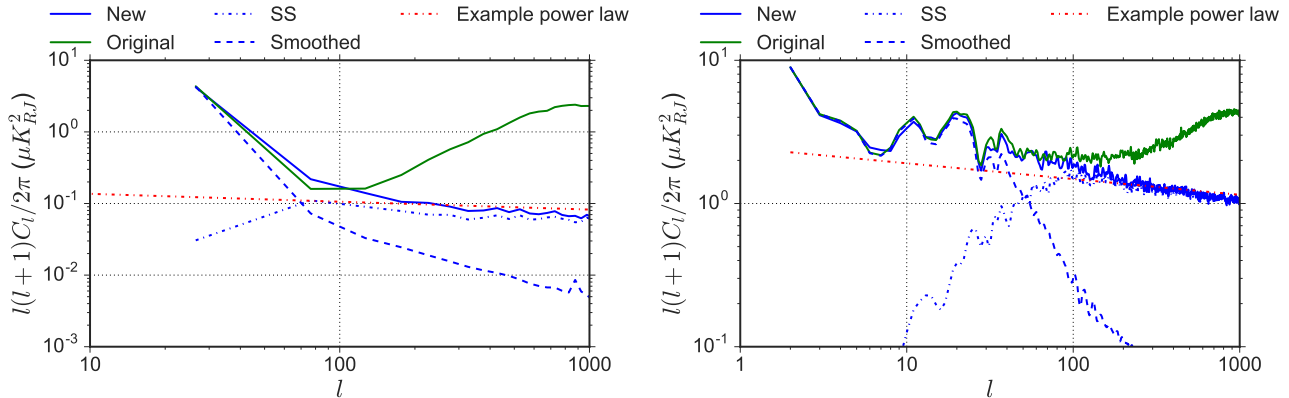


Figure 8. *Left:* dust BB spectra in the 825 square degree region centered on RA, DEC = [0, -55], as in Figure 7. *Right:* dust BB spectra in the Gal 80 region, as in Figure 7.

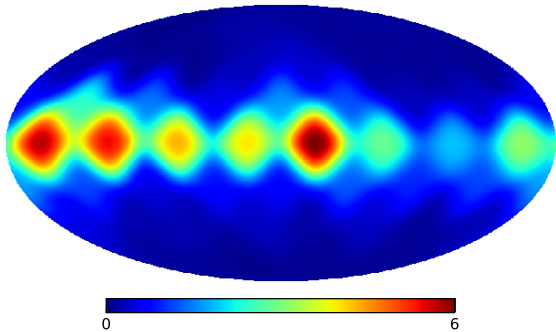


Figure 9. Normalization map, $N(\hat{\mathbf{n}})$, for the dust Q map.

3.3 Intensity: Free-free

The free-free template is smoothed at degree scales, which defines M_0 . We found the lognormal procedure to be unsuitable for generating small scales for the free-free maps, as the comparatively larger dynamic range in small patches caused the exponential term to yield unrealistically large variation on small scales. We also found the free-free angular spectrum to be flatter than the synchrotron, so a direct extrapolation

of the power law to smaller scales produced excess power at small scales that is likely not physical. We therefore fixed the gradient of the free-free power spectrum to be $\gamma = -0.5$, and used this to generate a δ_G realization with variance σ_G^2 . We then take the small scale map to be:

$$M_{\text{ss}}(\hat{\mathbf{n}}) = R(\hat{\mathbf{n}})\delta_G(\hat{\mathbf{n}}) \quad (19)$$

where $R(\hat{\mathbf{n}}) = \langle M_0 \rangle (M_0(\hat{\mathbf{n}}) / \langle M_0 \rangle)^\alpha / 4\sigma_G$. We find that $\alpha = 1.15$ is the best-fit value to recover the correct power law behaviour of the power spectrum in the range $200 < \ell < 1000$. We redraw δ_G for any negative pixels from additional full-sky realizations until we have positive values everywhere. This was necessary for $< 0.5\%$ of pixels. An example is shown in Figure 11.

3.4 Intensity: Thermal dust and anomalous microwave emission

The *Planck* thermal dust map has a power spectrum in the low-foreground [RA, DEC = 0, -55] region that falls off approximately as a power law. This indicates that the thermal dust intensity map is signal dominated in this high Galactic latitude region at small scales, and we do not add additional components.

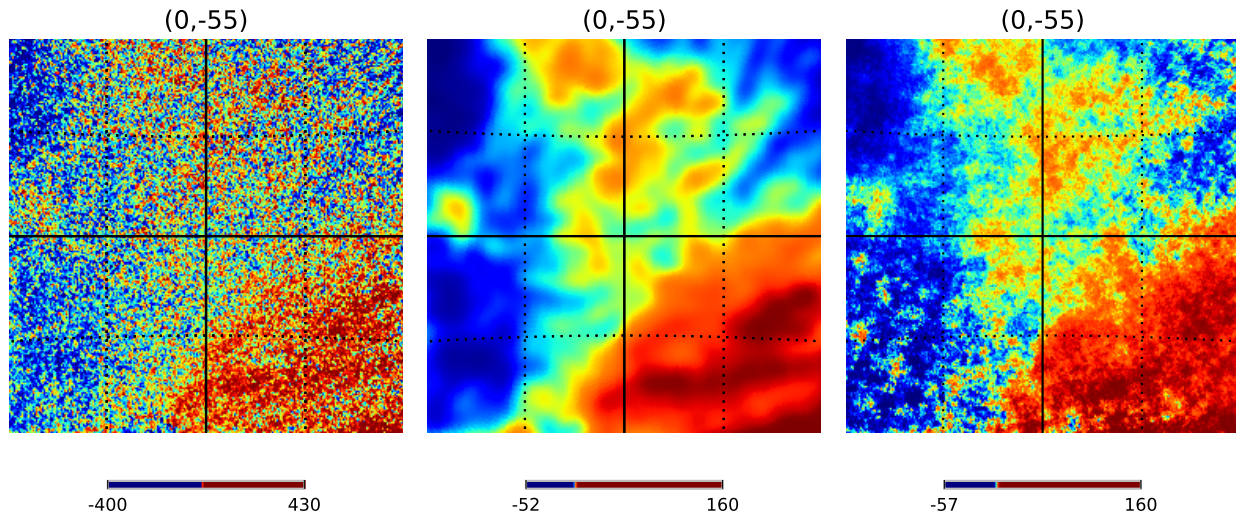


Figure 10. Gnomonic projection of dust Q maps in a patch centered at RA, DEC = (0, -55); 40 degrees to a side. The left panel is the original map, the middle panel has been smoothed (M_0), and the right hand panel has had small scales added ($M_0 + M_{ss}$). The maps are plotted in histogram-equalization in units of μK_{RJ} .

The AME templates are limited to degree resolution, so we use the high resolution thermal dust product as a proxy for the AME small scales. We produce the final AME map by multiplying the two intensity templates by the ratio of the high resolution thermal dust template and the dust template smoothed to one degree FWHM. An example is shown in Figure 11. The resulting AME templates therefore have the same small-scale morphology as the thermal dust template. Since the AME polarization templates are produced from the thermal dust polarization products we do not simulate AME polarization separately.

4 DISCUSSION

We have presented new software to simulate the Galactic microwave sky in polarization and intensity. The nominal models reflect the current understanding of Galactic foregrounds, and we have included a set of simple alternative models that capture physical extensions to these models and are still consistent with current data. There are many more possible alternatives that are not included, but we provide the public code in a way that makes adding further astrophysical complications straightforward. The code is also fast, portable, and easy to install and begin using.

We have developed methods for the addition of simulated small scale variation in polarization and intensity, recovering power law behaviour of the polarized components in sky patches of low and high signal, with minimal noise biasing. These simulations may aid in forecasting for ground-based observations limited to partial sky coverage. These small-scale simulations have certain limitations. Different simulated components are not correlated, and the small-scale procedure loses information in high signal-to-noise regions by smoothing at a single scale. Incorporating the spatially varying signal-to-noise into the definition of this smoothing scale would provide more accurate simulations.

The small-scales will also be non-Gaussian in practice, which we do not account for.

There are other approaches to foreground modelling. PySM uses 2D sky maps and parametric models to extrapolate single frequency maps to different frequencies. This will be limited in its ability to replicate the polarized nature of Galactic foregrounds. Due to the combination of the complex three-dimensional structure of the Galaxy’s magnetic field and the stacking of different sources along any given line of sight we may expect the polarization fraction of any component to be a function of frequency. Even on a microphysical level there is good evidence that the polarization spectrum of thermal dust is frequency dependent (e.g. Planck Collaboration et al. 2015c), as carbonaceous and silicate grains may align with the Galactic magnetic field with different efficiencies. More realistic simulations could be derived from three dimensional realizations of the Galaxy’s magnetic field and source distributions.

ACKNOWLEDGMENTS

BT acknowledges the support of an STFC studentship; JD and DA acknowledge the support of ERC grant 259505. DA acknowledges support from BIPAC. We thank Sigurd Næss for useful comments and for use of the `Taylens` code within PySM. We acknowledge use of the WMAP public maps on LAMBDA, the *Planck* public maps on the Planck Legacy Archive, the HEALPix software and analysis package (Górski et al. 2005), and the Planck Sky Model code (Delabrouille et al. 2013).

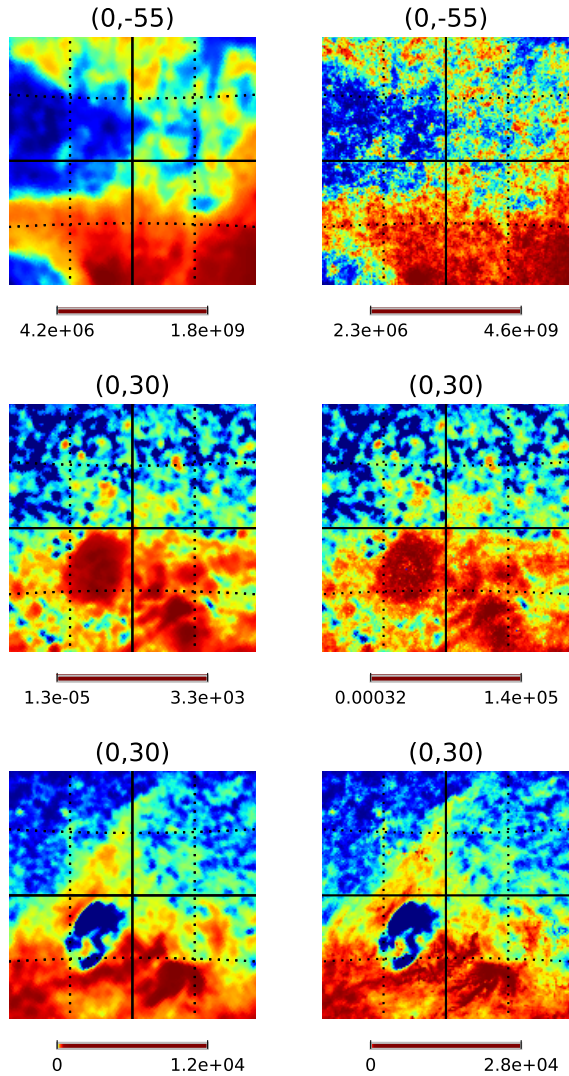


Figure 11. Synchrotron (top), free-free (middle), and AME (bottom) simulated intensity maps in a patch of side 40° centered at RA, DEC as indicated. Left: original template; right: simulation including small scales. These have been plotted in histogram-equalization to increase the dynamic range.

REFERENCES

- Ali-Haïmoud Y., Hirata C. M., Dickinson C., 2009, MNRAS, 395, 1055, [arXiv:0812.2904](#)
- B. Rybicki G., P. Lightman A., 1979, Radiative Processes in Astrophysics. Wiley
- Baumann D. et al., 2009. pp 10–120, [arXiv:0811.3919](#)
- Beck M. C., Beck A. M., Beck R., Dolag K., Strong A. W., Nielaba P., 2014, 1409.5120, [arXiv:1409.5120](#)
- Bennett C. L. et al., 2013, ApJS, 208, 20, [arXiv:1212.5225](#)
- BICEP2/Keck and Planck Collaborations et al., 2015, Physical Review Letters, 114, 101301, [arXiv:1502.00612](#)
- Chon G., Challinor A., Prunet S., Hivon E., Szapudi I., 2004, MNRAS, 350, 914, [arXiv:astro-ph/0303414](#)
- de Oliveira-Costa A., Kogut A., Devlin M., Netterfield C., Page L., Wollack E., 1997, ApJ, 482, L17+, [arXiv:9702172](#)
- de Oliveira-Costa A., Tegmark M., Gaensler B. M., Jonas J., Landecker T. L., Reich P., 2008, MNRAS, 388, 247, [arXiv:0802.1525](#)
- Delabrouille J. et al., 2013, A&A, 553, A96, [arXiv:1207.3675](#)
- Dickinson C., Peel M., Vidal M., 2011, MNRAS, 418, L35, [arXiv:1108.0308](#)
- Draine B. T., 2011, Physics of the interstellar and intergalactic medium. Princeton University Press
- Draine B. T., Lazarian A., 1998, ApJ, 508, 157, [arXiv:9802239](#)
- Draine B. T., Lazarian A., 1999, ApJ, 512, 740, [arXiv:9807009](#)
- Fauvet L. et al., 2011, A&A, 526, A145, [arXiv:1003.4450](#)
- Fauvet L., Macías-Pérez J. F., Désert F. X., 2012, Astroparticle Physics, 36, 57, [arXiv:1204.3659](#)
- Finkbeiner D. P., Davis M., Schlegel D. J., 1999, ApJ, 524, 867, [arXiv:9905128](#)
- Fraisse A. A. et al., 2009, in Dodelson S. et al., eds, American Institute of Physics Conference Series Vol. 1141, American Institute of Physics Conference Series. pp 265–310, [arXiv:0811.3920](#)
- Fuskeland U., Wehus I. K., Eriksen H. K., Næss S. K., 2014, ApJ, 790, 104, [arXiv:1404.5323](#)
- Génova-Santos R. et al., 2016, [arXiv:1605.04741](#)
- Gold B. et al., 2011, ApJS, 192, 15, [arXiv:1001.4555](#)
- Górski K. M., Hivon E., Banday A. J., Wandelt B. D., Hansen F. K., Reinecke M., Bartelmann M., 2005, ApJ, 622, 759, [arXiv:astro-ph/0409513](#)
- Haslam C. G. T., Klein U., Salter C. J., Stoffel H., Wilson W. E., Cleary M. N., Cooke D. J., Thomasson P., 1981, A&AS, 100, 209
- Haslam C. G. T., Stoffel H., Salter C. J., Wilson W. E., 1982, A&AS, 47, 1
- Hensley B. S., Draine B. T., Meisner A. M., 2015, [arXiv:1505.02157](#)
- Hervías-Caimapo C., Bonaldi A., Brown M. L., 2016, [arXiv:1602.01313](#)
- Hinshaw G. et al., 2013, ApJS, 208, 19, [arXiv:1212.5226](#)
- Hoang T., Lazarian A., Draine B. T., 2011, ApJ, 741, 87
- Ichiki K., 2014, Progress of Theoretical and Experimental Physics, 2014, 1
- Jansson R., Farrar G. R., 2012, ApJ, 757, 14, [arXiv:1204.3662](#)
- Kogut A., 2012, ApJ, 753, 110, [arXiv:1205.4041](#)
- Kogut A. et al., 2007, ApJ, 665, 355, [arXiv:0704.3991](#)
- Leitch E., Readhead A., Pearson T., Myers S., 1997, ApJ, 486, L23+, [arXiv:9705241](#)
- Lewis A., Challinor A., Lasenby A., 2000, ApJ, 538, 473, [arXiv:astro-ph/9911177](#)
- Macellari N., Pierpaoli E., Dickinson C., Vaillancourt J. E., 2011, MNRAS, 418, 888, [arXiv:1108.0205](#)
- Meisner A. M., Finkbeiner D. P., 2014, eprint 1410.7523, [arXiv:1410.7523v1](#)
- Miville-Deschenes M. A., Ysard N., Lavabre A., Ponthieu N., Macias-Perez J. F., Aumont J., Bernard J. P., 2008, A&A, 490, 1093, [arXiv:0802.3345v1](#)
- Næss S. K., Louis T., 2013, Journal of Cosmology and Astroparticle Physics, 9, 001, [arXiv:1307.0719](#)
- Orlando E., Strong A., 2013, MNRAS, 436, 2127, [arXiv:1309.2947](#)
- Planck Collaboration et al., 2015a, 1502.01582, [arXiv:1502.01582](#)
- Planck Collaboration et al., 2015b, 1502.01588,

- [arXiv:1502.01588](#)
Planck Collaboration et al., 2015c, A&A, 576, A107,
[arXiv:1405.0874](#)
Planck Collaboration et al., 2016, [arXiv:1606.07335](#)
Poh J., Dodelson S., 2016, ArXiv e-prints, [arXiv:1606.08922](#)
Remazeilles M., Dickinson C., Banday A. J., Bigot-Sazy
M. A., Ghosh T., 2014, eprint 1411.3628, 18, 1,
[arXiv:1411.3628v1](#)
Remazeilles M., Dickinson C., Eriksen H. K. K., Wehus I. K.,
2016, MNRAS, 458, 2032, [arXiv:1509.04714](#)
Ruud T. M. et al., 2015, ApJ, 811, 89, [arXiv:1508.02778](#)
Silsbee K., Ali-Haïmoud Y., Hirata C. M., 2011, MNRAS,
411, 2750, [arXiv:1003.4732](#)
Stevenson M. A., 2014, ApJ, 781, 113
Waelkens A., Jaffe T., Reinecke M., Kitaura F. S., Enßlin
T. A., 2009, A&A, 495, 697, [arXiv:0807.2262](#)
Zheng H., Tegmark M., Dillon J., Liu A., Neben A., Jonas
J., Reich P., Reich W., 2016, [arXiv:1605.04920](#)